Journal of
MARINE RESEARCH

Volume 66, Number 3

Continuously stratified nonlinear low-mode internal tides

by Karl R. Helfrich[1]

ABSTRACT

A model for hydrostatic, fully nonlinear, low-mode internal tides is extended to continuously stratified conditions. Periodic inertia-gravity solutions of permanent form are shown to exist only for a limited range of amplitudes for a given stratification and frequency. As found in an earlier two-layer model, the solutions fall into two classes. In one, the waves take on a corner-shape as the limiting amplitude is approached. In the other, the waves remain continuous at the limiting amplitude, but have a lobate shape. Numerical investigation using the Euler equations shows that both classes of nonlinear solutions are robust to weak nonhydrostatic effects representative of oceanic conditions. The numerical solutions are also used to explore the evolution of an initial sinusoidal internal tide. It is demonstrated that the presence of the nonlinear solutions may limit the disintegration of the initial tide into shorter solitary-like waves. The nonlinear tide solutions and the disintegration process are briefly explored for conditions of the northeastern South China Sea where large internal tides and solitary waves are observed.

1. Introduction

The generation of internal tides by barotropic tidal flow over topography has recently received much attention. Low-mode (principally mode-1) internal tides can propagate and remain coherent far (of order 10 wave lengths) from generation sites as shown by observations near the Hawaiian Ridge (Ray and Mitchum, 1996; Rainville and Pinkel, 2006a), the Indian Ocean (Lozovatsky *et al.*, 2003), and elsewhere (Ray and Mitchum, 1997). The internal tides are sinks of barotropic tidal energy and their dissipation, possibly quite remote from the generation site, may play an important role in the distribution of vertical mixing

1. Department of Physical Oceanography, Woods Hole Oceanographic Institution, Woods Hole, Massachusetts, 02543, U.S.A. ***email: khelfrich@whoi.edu***

(Wunsch and Ferrari, 2004). Thus the situations in which a low-mode internal tide can remain stable and propagate over a large distance is important.

Rainville and Pinkel (2006b) used a ray-tracing model to explore the role of refraction in variable ambient stratification and current fields and suggested that the internal tides were susceptible to enhanced dissipation at "baroclinic shoals" where wave energy is focused. At low latitudes, parametric subharmonic instability of the semi-diurnal tide (MacKinnon and Winters, 2005) has been proposed as a mechanism for the loss of energy from these low-mode tides. Another, perhaps more common mechanism, especially in coastal regions, involves nonlinear steepening of the long tide. Steepening leads to the transfer of energy to high wavenumbers where nonhydrostatic dispersion can balance the nonlinearity to produce packets of solitary-like waves (Lien *et al.*, 2005; Helfrich and Melville, 2006). The shorter solitary-like waves may then become unstable to shear instability or convective overturning.

In the absence of rotation, the time and space scales for the nonlinear steepening and production of the solitary-like waves can be estimated (Helfrich and Melville, 2006). However, at the length scale of the internal tide, rotation is fundamental. Using a weakly nonlinear, two-layer model Gerkema and Zimmerman (1995) and Gerkema (1996) showed that rotation can limit production of the short solitary waves. The reason is the presence, in the hydrostatic limit, of periodic nonlinear inertia-gravity (tidal) waves. These nonlinear waves arise through a balance between nonlinearity and low-frequency, rotational dispersion.

These nonlinear inertia-gravity wave solutions were first found by Ostrovsky (1978) in the hydrostatic limit of the rotationally modified, weakly-nonlinear KdV-equation. The inertia-gravity waves extend from the linear sinusoidal solution up to a limiting, maximum amplitude beyond which the rotational dispersion is unable to balance the nonlinearity. At fixed frequency or wavelength, increasing the amplitude causes the waves to depart from the linear sinusoidal form and become asymmetrical. The troughs (for a shallow upper layer in a two-layer stratification) become peaked and the crests broader. The maximum amplitude wave consists of a sequence of parabolic arcs joined together at a corner with discontinuous interfacial slope.

The weak nonlinearity of the Ostrovsky (1978), Gerkema and Zimmerman (1995) and Gerkema (1996) models is a potential limitation since observations often show that both the solitary waves and tides are strongly nonlinear with $\alpha = a/h_s = O(1)$. Here a is a measure of the wave amplitude and h_s is a vertical scale of the stratification (typically the water depth). This is particularly true in coastal settings (e.g., Stanton and Ostrovsky, 1998; Ramp *et al.*, 2005). This led Helfrich and Grimshaw (2008) to explore the disintegration of an initial sinusoidal internal tide in a two-layer model with full nonlinearity, $\alpha = O(1)$ and weak nonhydrostatic effects, $\beta = (h_s/l)^2 \ll 1$. Here l is the length scale of the flow. In the absence of nonhydrostatic effects, rotational dispersion could again balance the nonlinearity to give periodic inertia-gravity wave solution. These two-layer, hydrostatic, fully nonlinear solutions were first found by Plougonven and Zeitlin (2003) and extended and explored in Helfrich and Grimshaw (2008) as models of the internal tide. The two-layer solutions are extensions of the single-layer (reduced gravity) model developed by Shrira (1986) (also

see Grimshaw *et al.* (1998b)). With full nonlinearity, the two-layer inertia-gravity wave solutions were again limited to a maximum amplitude. The limiting corner waves (corner-class families of solutions) were present. However, full nonlinearity introduced a second class of solutions in which the wave profiles remained smooth at the limiting wave. This family was termed lobate-class. Only the corner-class waves appear in the single-layer model of Shrira (1986). Note that the Shrira (1986) model, if restricted to weak nonlinearity, can also describe corner-class waves for continuously stratified conditions that are related to the Ostrovsky (1978) solutions, but without the restriction to weak rotational effects.

Examples of both classes of the two-layer wave solutions for an undisturbed upper layer depth of $0.25H$, where H is the total depth are shown in Figure 1 (see Helfrich and Grimshaw (2008) for the model development). The corner-class waves in Figure 1a are for a frequency $\omega = 2f$, where f is the Coriolis frequency. As the wave amplitude is increased, the waves take on a peaked shape ending in a corner wave. The lobate-class waves are illustrated in Figure 1b for $\omega = 1.4f$. In both examples, the largest wave shown is close to the limiting amplitude. Which class occurs depends on the frequency (or wavelength). Shallow thermoclines and/or high frequencies lead to the corner-class waves. Generally, the lobate-class waves can be found over a larger range of amplitudes than the corner-class waves.

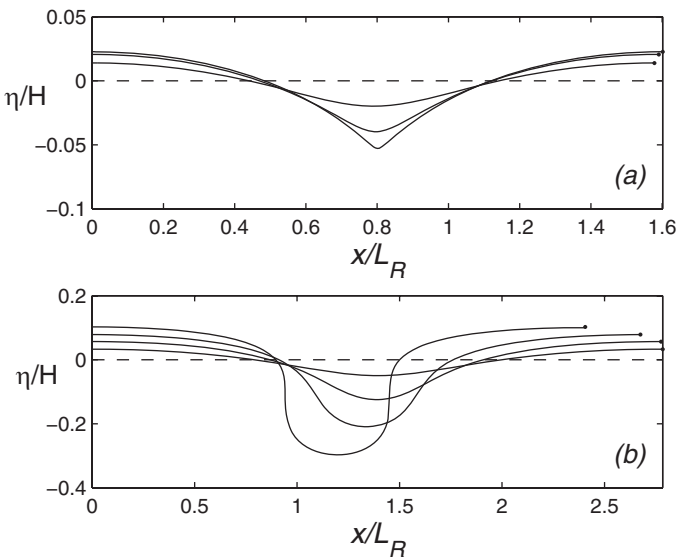

Figure 1. Examples of the two classes of hydrostatic, nonlinear inertia-gravity waves in a two-layer fluid with a mean upper layer depth of $0.25H$. The interfacial displacement η is shown over one wavelength. (a) Corner-class waves for $\omega = 2f$ with maximum interfacial displacements of $\eta/H = -0.02, -0.04$, and -0.056. (b) Lobate-class waves for $\omega = 1.4f$ and $\eta/H = -0.05, -0.125, -0.21$, and -0.3. The dots at the end of each wave profile indicate the wavelength. Here $L_R = \sqrt{g_0' H}/f$.

Helfrich and Grimshaw (2008) showed that these hydrostatic inertia-gravity waves are robust to weak nonhydrostatic effects and thus their presence plays a crucial role in the evolution of an initial sinusoidal internal tide. A nonlinear inertia-gravity wave may act as an attractor that completely inhibits the nonlinear steepening of the internal tide, or it may arrest the disintegration after some, but not all, of the energy in the initial tide is shed to the shorter solitary waves. The process involves a complex competition between nonhydrostatic (high-frequency) and rotational (low-frequency) dispersion to balance nonlinearity.

Given the important role these nonlinear waves play in the stability of low-mode internal tide and the production of solitary internal waves, the two-layer theory for fully nonlinear, hydrostatic inertia-gravity waves developed in Plougonven and Zeitlin (2003) and Helfrich and Grimshaw (2008) is extended to more realistic continuously stratified systems. The continuously stratified theory is developed in Section 2 and solutions are presented in Section 3 for several stratifications and other parameters (i.e., frequencies) representative of internal tides, including those in the South China Sea, a region of interest because of recent observations of very large internal tides and solitary waves. The role of weak nonhydrostatic effects are briefly explored in Section 4, again with an example relevant to the South China Sea. The results are summarized in Section 5.

2. Nonlinear tide theory

The situation under consideration is a continuously stratified fluid with background density profile $\bar{\rho}(z)$ rotating about the z-axis with Coriolis frequency f. The upper surface, $z = 0$, is a rigid lid and the bottom $z = -H$ is flat. Gravity g acts in the negative z direction. Waves propagate in the x direction and have no variations in the transverse, y, direction (i.e. $\partial/\partial y = 0$). The wavelength λ is very long with respect to the depth H such that the flow is hydrostatic, $\beta = (H/\lambda)^2 \to 0$. The flow is inviscid, Boussinesq, and governed by the primitive equations. It is most convenient to work in density coordinates since the terms in the momentum equations involving z derivatives are eliminated and the potential vorticity takes a simplified form. The governing equations are (Pedlosky, 1996)

$$u_t + uu_x - fv = -\mathcal{M}_x \tag{1}$$

$$v_t + uv_x + fu = 0 \tag{2}$$

$$(z_\rho)_t + (uz_\rho)_x = 0. \tag{3}$$

The ρ, x and t subscripts indicate partial differentiation (at fixed ρ for x and t). In this coordinate system the horizontal velocities $\mathbf{u} = \mathbf{u}(x, \rho, t)$ and the vertical position of an isoline of density $z = z(x, \rho, t)$ are functions of the density ρ. The Montgomery function

$$\mathcal{M} = \frac{p}{\rho_0} + \frac{g\rho z}{\rho_0}, \tag{4}$$

the pressure p is hydrostatic

$$p_z = -g\rho, \tag{5}$$

and ρ_0 is a reference density.

From (1)-(3) it is straightforward to show that the potential vorticity

$$q = -\frac{f + v_x}{z_\rho} \tag{6}$$

is conserved following fluid parcels. The minus sign is included since $z_\rho < 0$ for the stable stratifications considered.

For steadily propagating waves with phase speed c, the dependent variables are functions of $\xi = x - ct$. Thus (3) becomes $[(u - c)z_\rho]_\xi = 0$, and after integration in ξ, $(u - c)z_\rho = C(\rho)$. Here $C(\rho)$ is a constant of integration. For periodic waves with wavelength λ and zero net transport between any two isopycnals

$$\int_0^\lambda u z_\rho d\xi = 0.$$

Thus $C = -c\bar{z}_\rho$ and

$$(u - c)z_\rho = -c\bar{z}_\rho. \tag{7}$$

From (2) and (7)

$$v_\xi = f\left(\frac{z_\rho}{\bar{z}_\rho} - 1\right). \tag{8}$$

Using this result in (6), the potential vorticity is equal to the undisturbed background potential vorticity $q = -f/\bar{z}_\rho$.

Combining (8) with the ξ derivative of (1) gives

$$\frac{\partial^2}{\partial \xi^2}\left[\frac{(u - c)^2}{2} + \mathcal{M}\right] = f^2\left(\frac{z_\rho}{\bar{z}_\rho} - 1\right)$$

Taking the ρ derivative of this equation, using (7) and $\mathcal{M}_\rho = gz/\rho_0$ [from (4) and (5)] gives an equation for $z(\xi, \rho)$,

$$\frac{\partial^2}{\partial \xi^2}\left[\frac{c^2}{2}\frac{\partial}{\partial \rho}\left(\frac{\bar{z}_\rho}{z_\rho}\right)^2 + \frac{gz}{\rho_0}\right] = f^2\frac{\partial}{\partial \rho}\left(\frac{z_\rho}{\bar{z}_\rho}\right). \tag{9}$$

Eq. (9) is a single partial differential equation for the flow streamlines, in this case the position $z(\xi)$ of isolines of ρ. It bears some similarity to the Dubreil-Jacotin-Long equation for nonrotating stratified flow (c.f. Turner, 1973). Unlike the Dubreil-Jacotin-Long equation there appear to be no special nonlinear cases that are amenable to analytical methods. Therefore solutions are obtained numerically.

Before solutions to (9) are discussed, it is convenient to introduce the nondimensionalization

$$\sqrt{g_0' H} \to u, v, c, \quad H \to h, z, \quad l \to x, \quad l/\sqrt{g_0' H} \to t, \quad \rho_0 \to \rho. \tag{10}$$

Here $g_0' = g\Delta\rho/\rho_0$ is the reduce gravity based on the bottom to top density difference $\Delta\rho = \bar{\rho}(-H) - \bar{\rho}(0)$. The length scale l is arbitrary, though it will be set equal to the deformation radius $L_R = \sqrt{g_0' H}/f$. Thus time is time scaled by f^{-1} (and wave frequency by f). The nondimensional density is now

$$\rho = 1 + \frac{\Delta\rho}{\rho_0} s, \tag{11}$$

where $s(x, z, t) = [0, 1]$ is the scaled departure of the density from the reference value.

With (10) and (11), (9) becomes

$$\frac{\partial^2}{\partial\xi^2}\left[\frac{c^2}{2}\frac{\partial}{\partial s}\left(\frac{\bar{z}_s}{z_s}\right)^2 + z\right] = \gamma^2 \frac{\partial}{\partial s}\left(\frac{z_s}{\bar{z}_s}\right). \tag{12}$$

The parameter $\gamma = l/L_R = 1$ in the scaling introduced above, but is retained for generality.

a. Numerical solution technique

The water column is divided up into M uniform density layers in the vertical. The $M+1$ layer interfaces are at $z_{j-1/2}$, with $j = 1, 2, \ldots, M+1$. The upper surface $z_{1/2} = 0$ and bottom $z_{M+1/2} = -1$ are constants. The centered, second-order s derivative of any variable ϕ is

$$\left.\frac{\partial\phi}{\partial s}\right|_{j+1/2} = \frac{\phi_{j+1} - \phi_j}{s_{j+1} - s_j}.$$

The layer thickness

$$h_j = z_{j-1/2} - z_{j+1/2}, \tag{13}$$

therefore

$$\left(\frac{z_s}{\bar{z}_s}\right)_j = \frac{h_j}{H_j}.$$

Here H_j is the resting thickness of layer j. Substitution of these into (12) gives

$$\frac{\partial^2}{\partial\xi^2}\left[\frac{c^2}{2}\left(\frac{H_{j+1}^2}{h_{j+1}^2} - \frac{H_j^2}{h_j^2}\right) + (s_{j+1} - s_j) z_{j+1/2}\right] = \gamma^2\left(\frac{h_{j+1}}{H_{j+1}} - \frac{h_j}{H_j}\right),\ j = 1, \ldots, M-1 \tag{14}$$

which along with (13) results in a set of equations for $z_{j+1/2}$. The total depth constraint

$$\sum_{j=1}^{M} h_j = 1$$

is automatically satisfied; however, physically realistic solutions also require that the layer depths $h_j > 0$, or $z_{j-1/2} > z_{j+1/2}$ from (13).

It should be no surprise that (13) and (14) can be obtained by starting directly from an M-layer hydrostatic system rather than the continuous equations. However, this derivation

makes clear the equivalence, in the hydrostatic limit only, of the continuous and the layered formulations in the limit $M \to \infty$.

When $M = 2$, (14) can be reduced to a single first-order ordinary differential equation in ξ for the interface $z_{3/2}$. This equation is identical to the two-layer model in Plougonven and Zeitlin (2003) and Helfrich and Grimshaw (2008).

It is convenient to express the interface position $z_{j+1/2} = \bar{z}_{j+1/2} + \eta_{j+1/2}$, where $\eta_{j+1/2}(\xi)$ is the departure from the mean position $\bar{z}_{j+1/2} = -\sum_{l=1}^{j} H_l$. Then (13) becomes $h_j = H_j + \eta_{j-1/2} - \eta_{j+1/2}$, which can be introduced into (14) resulting in $M-1$ coupled equations for $\eta_{j-1/2}$ $(j = 1, \ldots, M-1)$.

If $\eta_{j+1/2} = \hat{\eta}_{j+1/2} \exp(ik\xi)$, where k is a horizontal wavenumber and $\hat{\eta}_{j+1/2}$ is an amplitude, is substituted into (13) and (14) and only linear terms are retained, (14) reduces to

$$H_j^{-1}\hat{\eta}_{j-1/2} - \left[H_j^{-1} + H_{j+1}^{-1} - \frac{s_{j+1} - s_j}{c^2 + \gamma^2 k^{-2}} \right] \hat{\eta}_{j+1/2} + H_{j+1}^{-1}\hat{\eta}_{j+3/2} = 0, \; j = 1, \ldots, M-1.$$

With the boundary conditions $\hat{\eta}_{1/2} = \hat{\eta}_{M+1/2} = 0$, this equation is a finite-difference approximation to the linear boundary value problem for hydrostatic, continuously stratified inertia-gravity waves

$$\eta_{zz} - \frac{\bar{s}_z}{c^2 + \gamma^2 k^{-2}} \eta = 0, \quad \eta(0) = \eta(-1) = 0.$$

The eigenvalue c, now denoted c_{0f}, is the linear phase speed of the wave with vertical mode number $n \geq 1$.

Nonlinear solutions are obtained by finite-differencing (14) in ξ using centered second-order differences. Since periodic waves are sought, one choice is to difference the equation over the wavelength λ and impose periodic boundary conditions. However, it is more efficient to solve over $0 \leq \xi \leq \lambda/2$ and impose $d\eta/d\xi = 0$ at each end. These conditions require that the waves remain smooth and are symmetric in ξ about the wave trough or crest. The latter is true of all the two-layer solutions (Plougonven and Zeitlin, 2003; Helfrich and Grimshaw, 2008). The first is true unless the solution is a limiting corner-class wave. In that case the slope $d\eta/d\xi$ is not known. The same issue would also occur in a periodic domain. However, smooth solutions up to any limiting corner-class waves can be found with either domain length. As shown below, the occurrence of a corner-wave can be deduced by the behavior of the numerical solutions.

Thus the horizontal grid $\xi_i = (i-1)d\xi$ with $i = 1, N+1$, and $d\xi = \lambda/(2N)$ is used. The result is a $(N+1) \times (M-1)$ nonlinear system of equations for $z_{i,j+1/2}$ (or $\eta_{i,j+1/2}$) is solved with the MatLab routine *fsolve*. The routine is initialized with the linear inertia-gravity wave solution and a phase speed c near c_{0f} is specified. The solution for the next value of c is found using the previous solution as the starting point. This gives a family of solutions at constant λ. Solution families at a fixed wave frequency ω are obtained by

setting $\lambda = 2\pi c/\omega$. Each solution for a new c is started from previous solution, with ξ rescaled by the new λ.

In addition to the requirement that all the layer depths $h_j > 0$, the periodicity of a solution gives, after integrating (8) over a wavelength and finite-differencing in s (ρ),

$$\int_0^\lambda h_j d\xi = \lambda H_j.$$

Since $h_j = H_j + \eta_{j-1/2} - \eta_{j+1/2}$ and $\eta_{1/2} = 0$, this becomes

$$\int_0^\lambda \eta_{j+1/2} d\xi = 0, \quad j = 1, M-1,$$

which is used to evaluate the acceptability of solutions.

3. Nonlinear solutions

To illustrate the nonlinear solutions the generic background stratification

$$\hat{s} = \frac{1}{2}(1 - \tanh[\alpha(z - z_0)]), \tag{15}$$

with

$$\bar{s} = \frac{\hat{s}(z) - \hat{s}(0)}{\hat{s}(-1) - \hat{s}(0)} \tag{16}$$

is employed. The normalization in (16) gives $\bar{s}(0) = 0$ and $\bar{s}(-1) = 1$. Density profiles for the parameters $(\alpha, z_0) = (12, -0.2)$ (case I) and $(6, -0.4)$ (case II) are shown in Figure 2. The second set of parameters leads to a deeper and thicker thermocline than the first set.

An example of a mode-1 wave for the case I stratification is show in Figure 3. The solution was computed with $M = 20$ and $N = 100$ (200 points in ξ per wavelength). The densities of the layer mid-points are marked by the small circles in Figure 2. The layers are non-uniform with thinner layers concentrated near the upper surface. This wave has frequency $\omega = 1.2$ and phase speed $c = 0.633$, which is less than the linear phase speed $c_{0f} = 0.643$. The figure shows contours of $s(\xi, z) = \bar{s}(\xi, z - \eta(\xi, z))$, and $u(\xi, z)$ and $v(\xi, z)$ velocities that have been mapped into the $\xi - z$ plane. The wave amplitude, or greatest interface displacement, $\eta_{MAX} = -0.0964$ at the wave trough ($\xi = \lambda/2 = 1.657$).

A larger wave with the same background stratification and frequency is shown in Figure 4. Here $c = 0.518$ and $\eta_{MAX} = -0.3270$. This wave has clearly taken on the lobe shape found in the two-layer model (c.f. Fig. 1b). An interesting feature of the velocity field, present in the previous example but clearer here, is the development of a "three-layer," or second vertical mode, flow just ahead of and behind the trough. The u velocities near $\xi \approx 1$ (1.7) are negative near the surface and at depth, but positive in the thermocline. Within the range $-0.34 < z < -0.17$ the velocity $u > 0$ for all ξ. The same is true, over a more restricted range in z, for the smaller wave in Figure 3. The emergence of the mode-2 structure in the

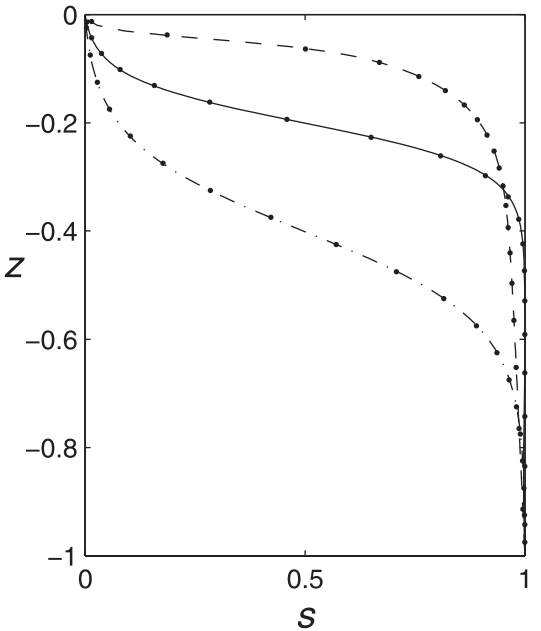

Figure 2. Background density profiles $\bar{s}(z)$. The solid line is from (15) with the case I parameters and the dashed-dot line is for case II parameters. The dashed line is the South China Sea stratification from (17). The small solid dots indicate the densities (at the mid-points) of the 20 layers used in the calculation of the nonlinear solutions.

u fields (it is not readily apparent in the corresponding s fields) is a consequence of the nonlinearity.

The dependence of phase speed on wave amplitude for $\omega = 1.2$ is shown in Figure 5a. As the wave amplitude increases, the phase speed decreases until $c = 0.491$ and $\eta_{MAX} = -0.364$, beyond which solutions cannot be found. This limiting wave has a lobate shape very close to that in Figure 4. Also shown in the figure are phase speeds for the same stratification and frequency with $M = 28$ and $N = 100$ and 150. Increasing M from 20 to 28 with $N = 100$, leads to nearly indistinguishable changes in the speed versus amplitude relation. Increasing N to 150 introduces a modest change for the largest waves. For the remainder of this section the resolution is set to $M = 20$ and $N = 100$, but note that there may be some dependence on resolution for very large waves near the limiting amplitude.

The locus of solutions with the case I background stratification and frequencies $\omega = 1.4$, 1.6, and 2 are also shown in Figure 5a. Increasing the frequency to $\omega = 1.4$ ($c_{0f} = 0.5077$) results in an increase of wave speed with amplitude. The $s(\xi, z)$ solution for the limiting wave, $c = 0.5276$ and $\eta_{MAX} = -0.1725$, is shown in Figure 6a. It is still in the lobate class, though the width of the trough is considerably narrower than for the $\omega = 1.2$ limiting wave. Increasing the frequency to $\omega = 1.6$ ($c_{0f} = 0.4452$) produces a

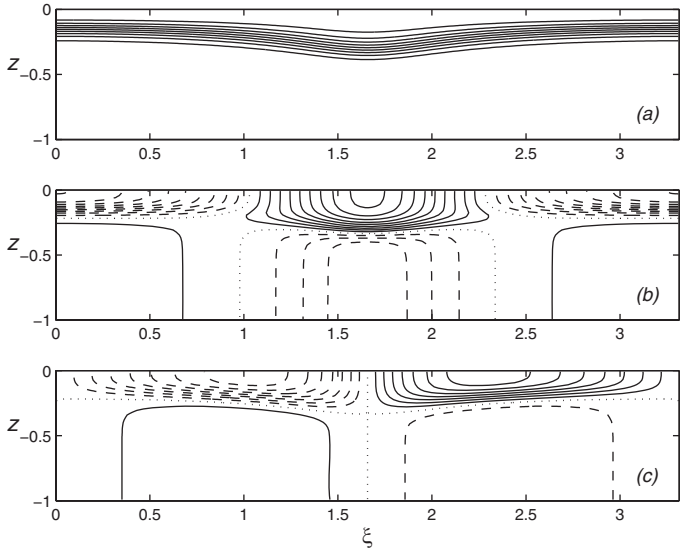

Figure 3. Nonlinear wave solution for case I stratification with $\omega = 1.2$ and $c = 0.633$. (a) s contoured in intervals of 0.1, (b) u, and (c) v. In both (b) and (c) the contour interval is 0.025. Positive velocities are solid, negative are dashed and the dotted line is the zero contour.

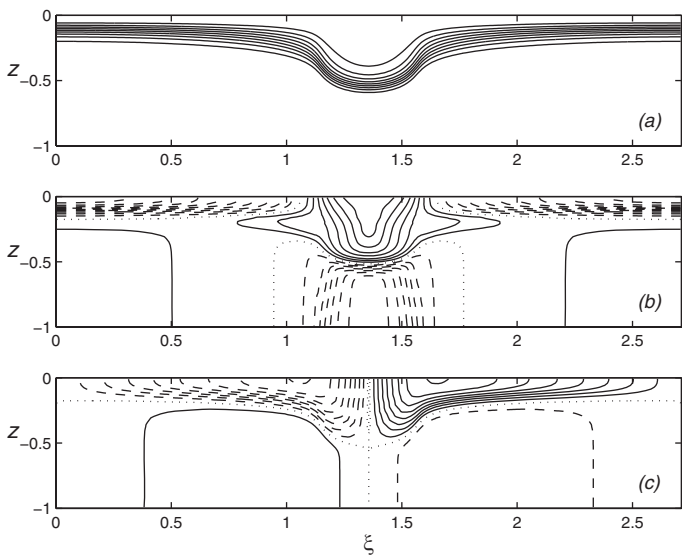

Figure 4. As in Figure 3 except $c = 0.518$.

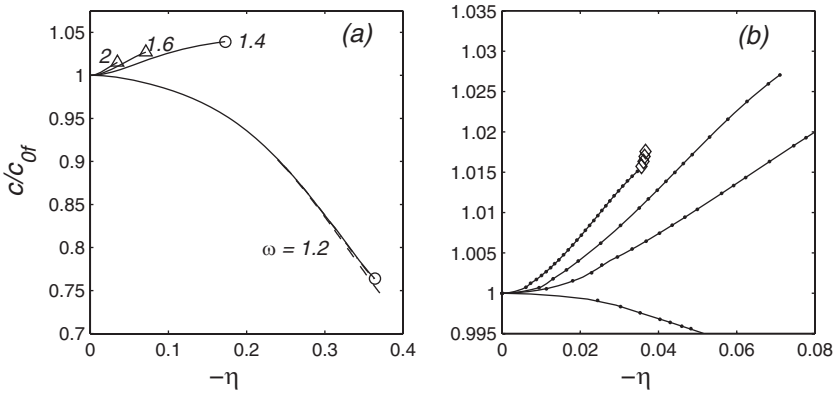

Figure 5. (a) The phase speed, c, versus amplitude, $-\eta_{MAX}$, for the case I stratification at $\omega = 1.2$, 1.4, 1.6, and 2. The speeds have been normalized by the linear phase speed $c_{0f} = 0.643$, 0.508, 0.445, and 0.410, respectively. The triangles (circles) indicate maximum waves in the corner (lobate) class. The dashed line for $\omega = 1.2$ is computed with $M = 28$ and $N = 150$. The curve for $M = 28$ and $N = 100$ is indistinguishable from the solid line. (b) A close-up of (a) showing the locations of nonlinear solutions (solid dots) and the spurious solutions for $\omega = 2$ (diamonds).

transition to a corner-class limiting wave. Figure 6b shows the $\omega = 1.6$ maximum wave which has $c = 0.4695$ and $\eta_{MAX} = -0.0751$. The s contours seem to be approaching a sharp corner, though as discussed earlier, a discontinuity in interface slope is difficult to resolve numerically. However, the behavior of the numerical solution near this point

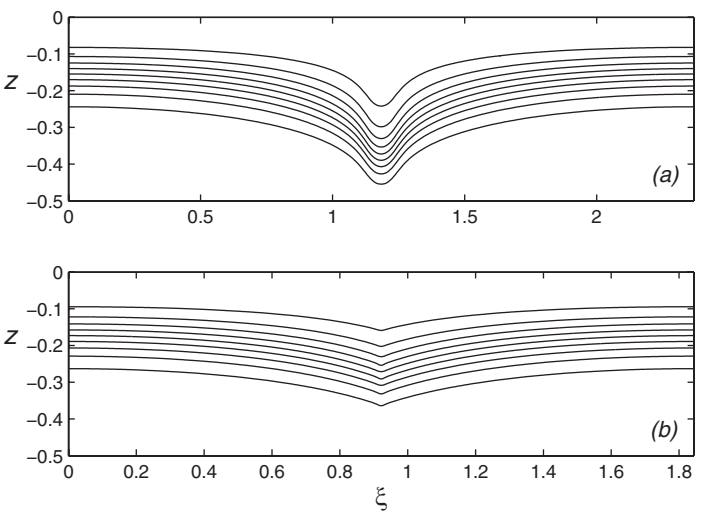

Figure 6. Contours of $s(\xi, z)$ for the limiting waves with case I stratification at (a) $\omega = 1.4$ and (b) $\omega = 1.6$. Note that only the upper half of the water column is shown. The contour interval is 0.1.

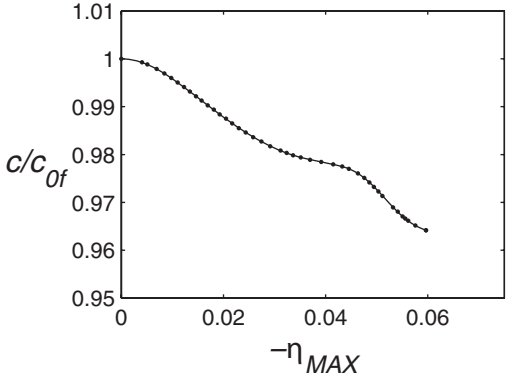

Figure 7. The phase speed, c, versus amplitude, η_{MAX}, for the mode-2 vertical structure waves with case I stratification and $\omega = 1.2$. The speed has been normalized by the linear phase speed $c_{0f} = 0.2043$.

indicates a change in behavior. Figure 5b shows a close-up of the dispersion curves. The small solid circles indicate acceptable solutions from the numerical procedure. The open diamonds shown for the $\omega = 2$ case indicate solutions that were deemed unacceptable for two reasons. First, they produced an abrupt change in the slope of the c versus amplitude curve. Second, examination of the solutions indicated that the only changes were within ± 2 grid points of the trough, rather than across the whole wave, suggesting a local resolution problem. There is, of course, some ambiguity about the determination of the limiting wave in these cases. Increasing the numerical resolution slightly changes the quantitative results, though not the qualitative conclusion of an approach to a limiting corner-class wave.

The result shown in Figure 5 of increasing ω leading to a transition from lobate to corner-class waves and with decreasing range of solution amplitudes are both consistent with the two-layer model (Helfrich and Grimshaw, 2008) and illustrated in Figure 1.

A new aspect of the continuous model is the possibility of higher vertical modes. Figure 7 shows the locus of mode-2 nonlinear solutions for $\omega = 1.2$ and the case I stratification ($c_{0f} = 0.2035$). Two of these solutions, including the limiting wave, are shown in Figure 8. As found in the mode-1 solutions at $\omega = 1.2$, the limiting wave is in the lobate class. However, compared to the mode-1 solutions at the same frequency, the range of mode-2 solution amplitudes is much more limited. Indeed, it is not possible to find solutions for $\omega = 1.4$ due, apparently, to the rapid decrease of the range of solutions.

Dispersion curves for mode-1 solutions with the deeper and more diffuse case II stratification are shown in Figure 9 for $\omega = 1.4$, 2, and 2.6 ($c_{0f} = 0.5843$, 0.4722, and 0.443, respectively). In these examples all the limiting waves are in the lobate class. Two of the solutions for $\omega = 2$ are shown in Figure 10. The waves develop very long, flat troughs. Again the behavior of the c versus amplitude curves and the development of broad troughs is consistent with the two-layer model when the pycnocline approaches the mid-depth of the water column.

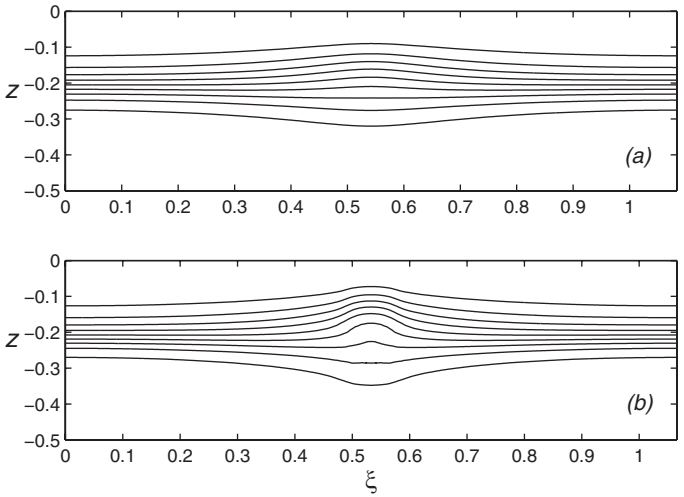

Figure 8. Contours of $s(\xi, z)$ for mode-two waves with case I stratification at $\omega = 1.2$ with (a) $\eta_{MAX} = 0.0312$ and $c = 0.207$ and (b) the limiting wave with $\eta_{MAX} = 0.0596$ and $c = 0.2035$. Note that only the upper half of the water column is shown. The contour interval is 0.1.

a. An example: South China Sea

There has recently been much interest in the internal tides and large-amplitude internal solitary-like waves observed in the northeastern South China Sea (Ramp *et al.*, 2005; Zhao and Alford, 2006). The large solitary waves with amplitudes of $100 - 150$ m emerge from the steepening of the internal tide as it propagates west across the basin from the generation site neat the Batan Island in the Luzon Strait to the continental shelf, a distance of about

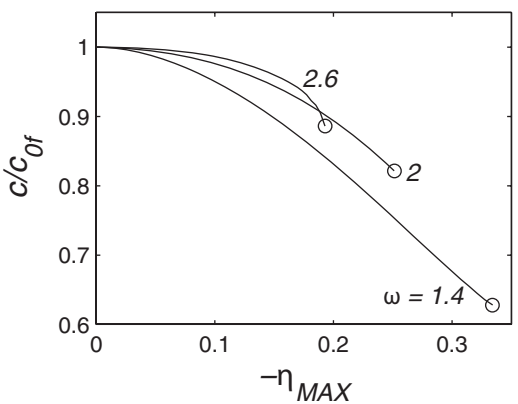

Figure 9. The phase speed, c, versus amplitude, $-\eta_{MAX}$, for the case II stratification at $\omega = 1.4$, 2, and 2.6. The speeds have been normalized by the linear phase speed $c_{0f} = 0.5843$, 0.4722, and 0.4430, respectively. The circles indicate that the maximum waves are in the lobate-class.

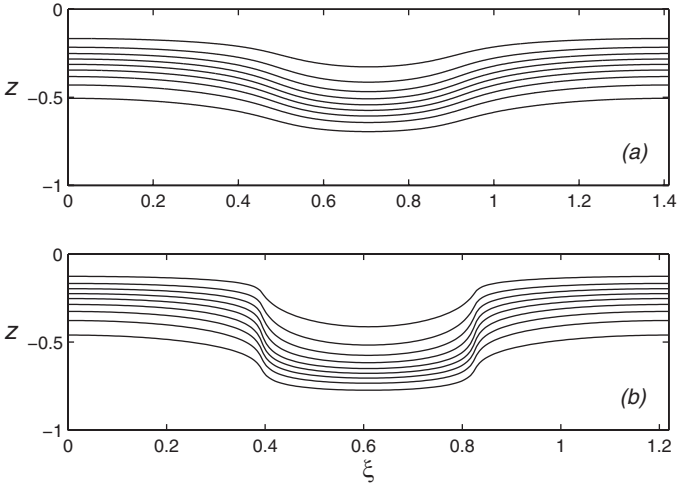

Figure 10. Contours of $s(\xi, z)$ for waves with case II stratification at $\omega = 2$ with (a) $\eta_{MAX} = -0.1416$ and $c = 0.4490$ and (b) $\eta_{MAX} = -0.2511$ and $c = 0.3880$. The contour interval is 0.1.

500 km (Zhao *et al.*, 2004; Lien *et al.*, 2005). Thus it is useful to explore the nonlinear tide solutions for a continuous stratification representative of the South China Sea.

The mean summer stratification in the central basin of the northeastern South China Sea is well approximated by $\bar{s}(z)$ from (16) with

$$\hat{s}(z) = (1 - \tanh[\alpha_1(z - z_0)]) \left[\frac{1 - e^{\alpha_2 z}}{1 - e^{-\alpha_2}} - az \right] \tag{17}$$

and $(\alpha_1, z_0, \alpha_2, a) = (50, -0.04, 14, 0.06)$. This stratification, plotted in Figure 2, has been nondimensionalized using $g_0' = 0.0554$ m s^{-2} and $H = 3000$ m from the surface to bottom density difference and nominal depth.

The generating barotropic tides at Luzon are mixed with comparable diurnal (K1) and semi-diurnal (M2) amplitudes (Ramp *et al.*, 2005; Zhao and Alford, 2006). At 21N, the nondimensional frequencies are $\omega = 1.4$ and 2.7 for the diurnal and semidiurnal tides, respectively.

Figure 11 shows the range of nonlinear internal tide solutions computed with (17) at the $\omega = 1.4$ diurnal frequency. The solutions exist up to a maximum amplitude $\eta_{MAX} = -0.0305$ and $c = 0.329$ ($c_{0f} = 0.3158$). The limiting wave is in the corner class and is shown in Figure 12. It was not possible to find nonlinear solutions at the semi-diurnal frequency $\omega = 2.7$. If they exist, it must be over a very much smaller range than the diurnal solutions since increasing frequency always leads to a reduced range of allowable amplitudes (c.f. Fig. 5a).

These continuously stratified solutions should be compared to the two-layer nonlinear tide solutions in Helfrich and Grimshaw (2008). They used the same stratification (17) and found that the linear eigenmode has a maximum at $z \approx -0.2$ and a zero in the horizontal

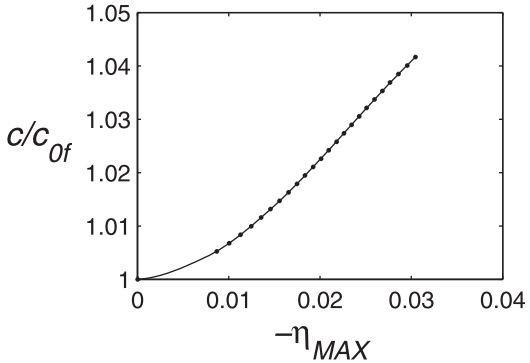

Figure 11. The phase speed, c, versus amplitude, $-\eta_{MAX}$, for the South China Sea stratification at $\omega = 1.4$. The speed has been normalized by the linear phase speed $c_{0f} = 0.315$.

velocities at this depth. (This is evident in Fig. 12b and c which show zeros in the velocity fields at $z \approx -0.2$.) Accordingly, they set the nondimensional mean upper layer depth to 0.2 and computed the nonlinear solutions for $\omega = 1.4$ and 2.7. The diurnal solutions were in the lobate-class and could be found for quite large amplitudes ($\eta_{MAX} = -0.293$). The semi-diurnal solutions were in the corner-class and had a much smaller maximum amplitude ($\eta_{MAX} = -0.0159$).

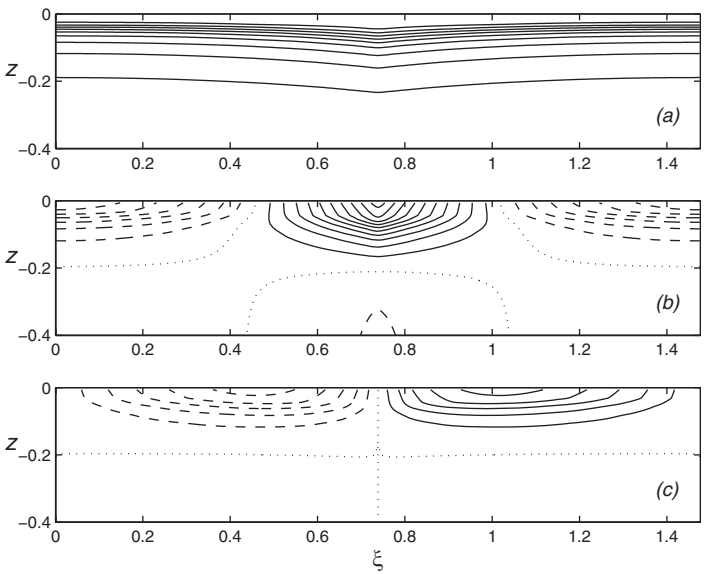

Figure 12. The limiting nonlinear wave solution for South China Sea stratification with $\omega = 1.4$. (a) s contoured in intervals of 0.1, (b) u, and (c) v. In both (b) and (c) the contour interval is 0.01. Positive velocities are solid, negative are dashed and the dotted line is the zero contour. Note that only the upper part of the water column is shown.

The differences between the continuously stratified solutions and the two-layer model are substantial. They appear to be the result of the strongly surface-trapped character of the stratification, despite the zero-crossing of the horizontal velocities at $z \approx -0.2$. In the two-layer model, a decrease of the upper layer depth, at a fixed frequency, leads to a reduction of the allowable range of solutions and the possibility of a transition from lobate to corner-class limiting waves. If the undisturbed upper-layer depth in the two-layer model is set to 0.08, which is where $\bar{s} = 0.63$ in Figure 2, the diurnal internal tide is in the corner class and has a maximum amplitude $\eta_{MAX} = -0.0302$, quite close to the continuously stratified result. The maximum semi-diurnal solution is also a corner-wave with a much smaller amplitude $\eta_{MAX} = -0.0051$. Choosing the mean interface to be where $\bar{s} = 0.5$ gives a mean upper layer depth of 0.064. The limiting diurnal nonlinear tide solution is again a corner wave with $\eta_{MAX} = -0.0231$, now substantially less than the continuous model. This exercise serves to emphasize the limitations of using a two-layer model to approximate a continuous stratification. It is possible to bring the two-layer and continuous stratification models into general agreement, but the best choice for the mean interface level is not obvious in the absence of the continuously stratified nonlinear solutions. Furthermore, the choice for the undisturbed interface position in the two-layer model will have important consequences for the properties of the shorter solitary waves that are produced from the tide.

4. Nonhydrostatic effects

The nonlinear inertia-gravity waves are found assuming hydrostatic flow. This is reasonable given that the length scales of the waves are very much greater than the water depth. However, it is possible that the waves are not robust to weak nonhydrostatic effects. For example, nonhydrostatic effects must be important locally near the crest of the limiting corner-type waves (Ostrovsky, 1978). Another important issue is the role that these nonlinear inertia-gravity waves play in the emergence of shorter, nonhydrostatic solitary-like waves from a general, long length-scale, initial condition. Weakly-nonlinear theories (Gerkema and Zimmerman, 1995; Gerkema, 1996) and fully nonlinear two-layer models (Helfrich and Grimshaw, 2008) have shown that the presence of hydrostatic, nonlinear internal tides (i.e., inertia-gravity waves) play a critical role in the disintegration of the tide and emergence of the short solitary waves. Here it is shown that, as in the two-layer model, the fully-nonlinear inertia-gravity waves are both robust to weak nonhydrostatic effects and can limit the disintegration of the internal tide.

The inviscid nonhydrostatic equations governing the rotating flow in the same system as (1)-(3) with $\partial/\partial y = 0$ are

$$u_t + uu_x + wu_z - \gamma v = -p_x \tag{18}$$

$$v_t + uv_x + wv_z + \gamma u = 0 \tag{19}$$

$$\beta(w_t + uw_x + ww_z) = -p_z - s \tag{20}$$

$$u_x + w_z = 0 \tag{21}$$

$$s_t + us_x + ws_z = 0. \tag{22}$$

The velocities u, v, and w are now functions of z, rather than the density coordinate system of (1)-(3). These equations are nondimensionalized with the scaling in (10) and $\beta^{1/2}\sqrt{g_0' H}$ for the vertical velocity w. The parameter $\beta = (H/l)^2$ (where the vertical scale h_s is set to H) is a measure of the nonhydrostatic effects, that for the scales of interest (either the long inertia-gravity waves or internal solitary waves) is small. The pressure p has been scaled by $\Delta\rho g H$. As earlier, $\gamma = l/L_R$. The two parameters, β and γ, can be reduced to one by taking l to be either L_R or H. Since the focus is on the evolution of the long internal tide, the choice $l = L_R$ is made, giving $\gamma = 1$ and $\beta^{1/2} = H/L_R$ as the sole remaining parameter. The nonlinear inertia-gravity waves then have length scales of $O(1)$ and any solitary-like waves will be much shorter. Typical values of $H = 50 - 3000$ m (coastal to deep ocean), $f \approx 10^{-4}$ s^{-1}, and $g' = 0.01$-0.05 m s^{-2} give $\beta^{1/2} = H/L_R = [0.4 - 5] \times 10^{-2}$ as representative of oceanic conditions.

Eqs. (18)–(22) are solved with the second-order projection method described by Bell and Marcus (1992). Because of the Godunov-type evaluation of the nonlinear terms the method is stable, requires no explicit dissipation, and introduces significant numerical dissipation only when large gradients (e.g. shocks) occur on the grid scale. Extension of the method to include rotation follows Lamb (1994), who demonstrated the effectiveness of the numerical scheme in problems of this type. The solutions presented below are periodic in x over one wavelength of the initial wave and have impermeable boundaries at $z = 0$ and -1. The numerical resolution depends on the particular case, but varies from $500 - 2000$ points in x. Between $50 - 100$ points were distributed in z to resolve the stratification. The highest resolutions are used in those runs in which short solitary-like waves emerge.

a. Numerical solutions

The stability of a nonlinear inertia-gravity wave to weak nonhydrostatic effects is illustrated in Figure 13. Figure 13a shows the density field for the initial wave with case I stratification parameters, $\omega = 1.2$, $\eta_{MAX} = -0.203$ and $c = 0.6$. These parameters place the wave between those shown in Figures 3 and 4. The nonhydrostatic model is integrated with $\beta^{1/2} = 0.04$ and the solution after eight periods, $t = 16\pi/\omega$, is plotted in Figure 13b. There is noticeable distortion of the wave, particularly near the crest. Although overall, the initial wave has remained intact. The amplitude is about the same and the phase propagation is only slightly less than the nonhydrostatic theory.

Two more examples of waves after eight periods of propagation with $\beta^{1/2} = 0.04$ are shown in Figure 14. The initial conditions for these nonhydrostatic solutions are the limiting amplitude waves shown in Figure 6. Again, both remain essentially unchanged, though in Figure 14b the corner at the wave crest has been slightly smoothed, as to be expected, by the addition of nonhydrostatic effects.

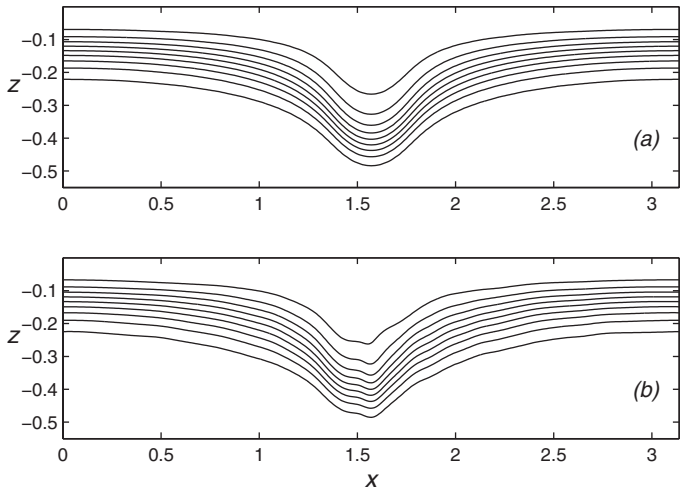

Figure 13. The evolution of a hydrostatic, nonlinear inertia-gravity wave in the presence of weak nonhydrostatic effects. (a) Contours of s for the initial wave with case I stratification, $\omega = 1.2$, $\eta_{MAX} = -0.203$, and $c = 0.6$. (b) The nonhydrostatic numerical solution with $\beta^{1/2} = 0.04$ at $t = 16\pi/\omega$. The contour interval is 0.1.

The value of $\beta^{1/2} = 0.04$ used in these three examples is at the high end reasonable estimates. Smaller values result in even less distortion of the wave. As in the two-layer theory, the nonlinear inertia-gravity waves are quite robust to weak nonhydrostatic effects.

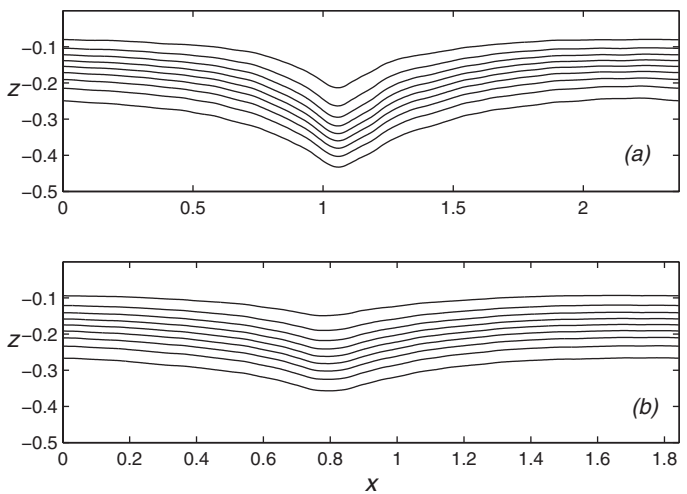

Figure 14. Contours of s from nonhydrostatic numerical solutions with $\beta^{1/2} = 0.04$ at $t = 16\pi/\omega$. Initial conditions are given by Figure 6a for (a) and Figure 6b for (b). The contour interval is 0.1.

The role of the hydrostatic solutions in the evolution of an initial sinusoidal disturbance is demonstrated with the stratification (17) for the South China Sea. A linear solution is used for the initial condition for purposes of illustration. Using the values for g_0', H and f from earlier, the deformation radius $L_R = \sqrt{g_0' H}/f = 247$ km and the nonhydrostatic parameter $\beta^{1/2} = 0.0121$. The initial condition for a calculation is the linear internal tide at the diurnal, $\omega = 1.4$ ($\lambda = 1.414$), or semidiurnal, $\omega = 2.7$ ($\lambda = 0.552$), frequency. Recall from Figure 11 that the maximum nonlinear tide solution has an amplitude $\eta_{MAX} = -0.0305$ (91.5 m when dimensionalized with H) and that nonlinear solutions could not be found for $\omega = 2.7$. Three amplitudes of the initial linear tide, measured by the maximum vertical isopycnal displacement, considered were 0.0083, 0.0167, and 0.025 (25, 50 and 75 m).

Figure 15 shows the nonhydrostatic solutions for $\omega = 1.4$ with these three amplitudes. The velocity u at the upper surface $z = 0$ is shown every quarter period of the linear tide over four periods in a reference frame moving with the linear phase speed $c_{0f} = 0.315$ of the initial condition. The surface velocity in the x direction allows a compact presentation of

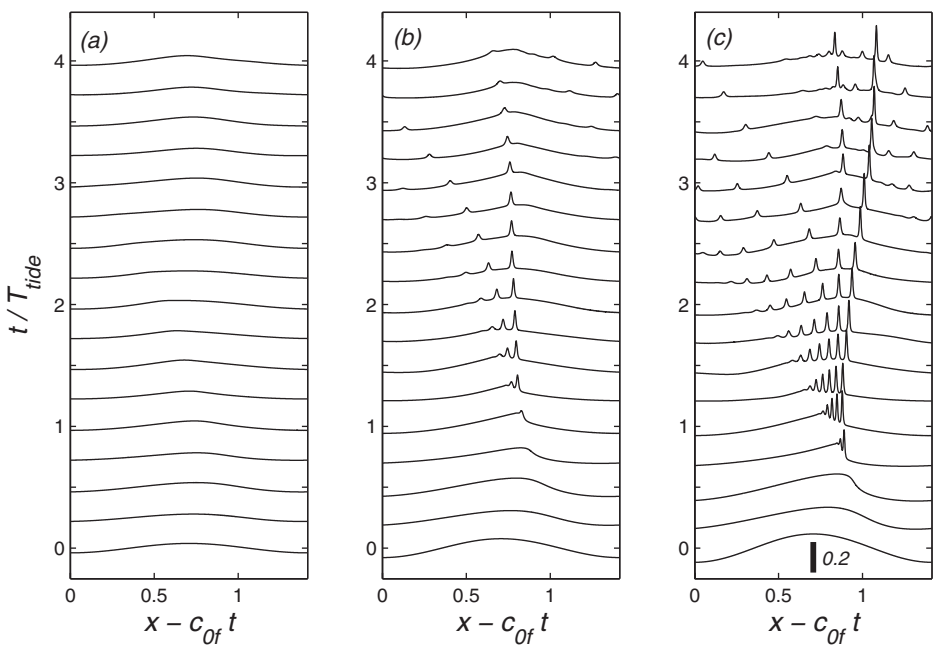

Figure 15. Nonhydrostatic evolution of an initial linear internal tide for the South China Sea stratification at the diurnal frequency $\omega = 1.4$ and $\beta^{1/2} = 0.0121$. The initial amplitude measured by maximum isopycnal displacement is (a) 0.00833 (25 m), (b) 0.0167 (50 m), and (c) 0.025 (75 m). The horizontal velocity u at $z = 0$ is plotted every quarter period of the linear tide $T_{tide} = 2\pi/\omega$. The solutions are shown in a frame moving to the right with the linear phase speed $c_{0f} = 0.315$. The solid vertical bar in (c) indicates the scale for u that is the same for all panels.

the evolution. Since the velocity fields of the (linear and nonlinear) tide solutions with this stratification are surface intensified (see Fig. 12) the surface velocity nicely encapsulates the internal wave field. The same surface intensification of internal solitary waves can also be show to occur. Positive velocities correspond to depressions of the isopycnals. The three panels of the figure show the evolution as the amplitude of the initial sinusoidal wave is increased. For the smallest amplitude (Fig. 15a) the initial tide evolves away from the pure sinusoidal initial condition, but does not steepen and no short solitary waves are produced. Increasing the initial amplitude to 50 m (Fig. 15b) causes the tide to steepen. After about one period nonhydrostatic dispersion begins to arrest the steepening and a packet of short, solitary-like waves emerges and then disperses. The disintegration of the initial tide, though, is incomplete. A substantial longwave component of the flow remains at the end of the calculation. Another interesting aspect of the solution is the emergence and then the apparent decay of the shorter solitary waves. The largest solitary wave at $t/T_{tide} = 2$ has a maximum isopycnal displacement of -0.045 (-135 m). However, from $t/T_{tide} = 2$ to 4 the wave rapidly decays. This is due, in part, to modulation by the velocity field of the long wave. It may also be a manifestation of the radiation decay of the solitary wave (Grimshaw *et al.*, 1998a; Helfrich, 2007). The important point is that the solitary waves produced by the steepening of the internal tide can be ephemeral. Energy is transfered from long- to short-wave components, and then back.

When the initial amplitude is increased to 75 m (Fig. 15c) the production of short solitary waves increases. The largest, leading solitary wave has isopycnal displacements of about -180 m. However, the disintegration of the initial tide is still arrested. Indeed, the long wave part of the solution after four tidal periods is similar to the solutions in Figures 15a and b.

This is shown in more detail in Figure 16 where the surface ($z = 0$) horizontal velocities, u and v, are shown at $t/T_{tide} = 4$ for the three examples in Figure 15. The transverse, v, velocity field is useful because it acts as a low-pass filter and tends to highlight the longer inertia-gravity waves since the shorter nonhydrostatic waves tend to have a weak expression in v (Gerkema, 1996; Gilman *et al.*, 1996). Also shown by the dashed lines are hydrostatic, nonlinear inertia-gravity wave solutions for the stratification and wavelength of the full nonhydrostatic solutions in Figure 15. The nonlinear inertia-gravity waves are members of a continuous family (see Fig. 11 for the family at fixed frequency $\omega = 1.4$, rather than fixed wavelength $\lambda = 1.414$) between the linear wave and the limiting wave. It is not possible to predict which, if any, of these waves the long wave part of the nonhydrostatic solution will fall upon. However, the minimum v in each of the three the nonhydrostatic solutions was used to select the theoretical inertia-gravity waves shown in Figure 16. The phase of the theoretical solutions was adjusted to approximately match the phase of the nonhydrostatic solutions. The agreement between the long wavelength part of the nonhydrostatic solutions (both u and v) and the theoretical solutions is quite good, especially for the 25 and 50 m initial linear tide amplitude cases. The largest, 75 m, case (Fig. 16c,f) also shows generally good agreement except in v in the neighborhood of the two large solitary waves ($x \approx 0.8$

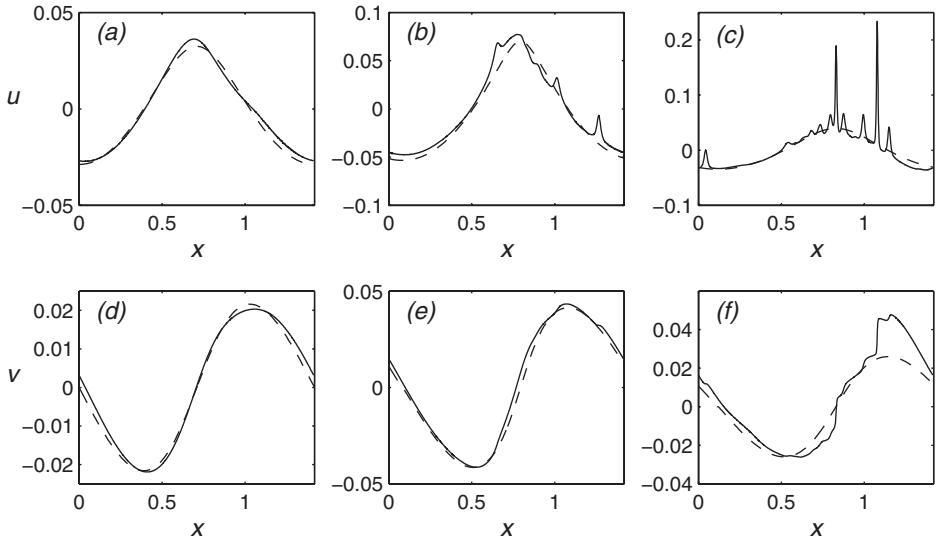

Figure 16. The solid lines in (a), (b) and (c) show u at $z = 0$ and $t/T_{tide} = 4$ for the numerical solutions in Figure 15a,b, and c respectively. Panels (d), (e), and (f) show (solid lines) the corresponding transverse velocity v at $z = 0$ for the solutions in (a), (b), and (c), respectively. The dashed lines in each panel show u and v at $z = 0$ for a nonlinear inertia-gravity wave solution with the same stratification and wavelength as the numerical runs. The inertia-gravity wave solution was selected by matching to the minimum v in each corresponding numerical solution.

and 1.05) where the solitary waves cause abrupt jumps in v as expected (Grimshaw *et al.*, 1998a). This indicates a continued strong interaction between the short solitary waves and the inertia-gravity wave part of the flow.

The important role of these nonlinear tide solutions is further emphasized in Figure 17 where the initial linear waves are at the semidiurnal frequency $\omega = 2.7$. For all three initial amplitudes the tides steepen until nonhydrostatic dispersion becomes important, after which packets of short solitary-like waves are formed. The amplitudes and number of waves increase with the initial tide amplitude. At the end of each calculation there is little evidence of a substantial long wave signal. This is consistent with the result in the previous section that at this frequency (or wavelength) nonlinear tide solutions either do not exist, or their amplitude range is very limited. Without the nonlinear tide solutions to arrest the disintegration, the initial tide energy is deposited into the short solitary-like waves.

Thus, as in the Helfrich and Grimshaw (2008) two-layer study, the presence, or absence, of a hydrostatic nonlinear inertia-gravity wave solution will stronly influence the degree of disintegration of the initial tide into shorter solitary waves. However, it is not yet possible to predict which wave (or waves) of the continuous family at the given wavelength, or frequency, the solution will settle upon.

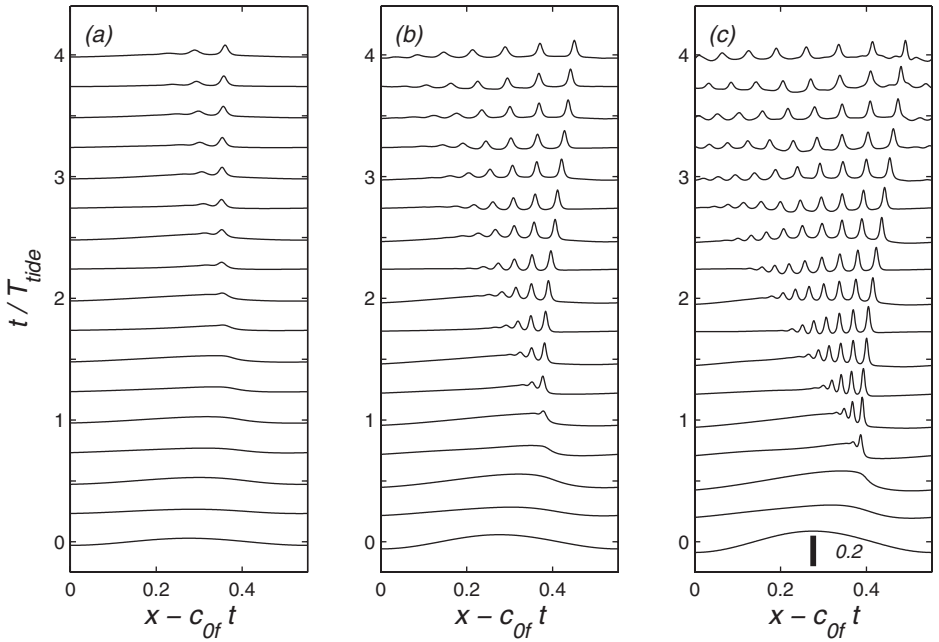

Figure 17. As in Figure 15 except for the semidiurnal frequency $\omega = 2.7$ where $c_{0f} = 0.237$.

5. Summary

The two-layer, fully nonlinear model for hydrostatic inertia-gravity waves (i.e., tides) (Plougonven and Zeitlin, 2003; Helfrich and Grimshaw, 2008) has been extended to continuously stratified fluids. In most respects the solution properties follow the two-layer results. Both corner-class and lobate-class waves are found. For mode-1 waves and a given stratification, increasing the wave frequency causes the range of solution amplitudes to decrease and leads to a change from a lobate- to corner-class solutions. Nonlinear solutions in the two-layer model can be found for all super-inertial frequencies. However, for continuous stratification, nonlinear solutions either ceased to exist or become very difficult to find numerically with increasing frequency. Higher (i.e. second) vertical mode solutions can be found, though their solution range is, for the few cases explored, much reduced from the mode-1 waves at the same frequency, and only lobate-class solutions have been found.

The nonlinear inertia-gravity wave solutions are robust to weak nonhydrostatic effects representative of oceanic conditions. As a consequence, the nonlinear disintegration of an initial sinusoidal tide can be arrested as the solution settles onto a nonlinear inertia-gravity wave solution after shedding some energy to shorter solitary waves. This was illustrated with an example using the stratification from the northeastern South China Sea where nonlinear tide solutions could be found at the diurnal tidal frequency, but not at the semi-diurnal frequency. In the diurnal case the initial tide needed to be above a threshold amplitude

(between 25 and 50 m) before partial disintegration took place. In contrast, at the semidiurnal frequency disintegration of the initial tide into shorter internal waves was nearly complete for all initial amplitudes considered. While not surprising in light of the earlier weakly- (Gerkema and Zimmerman, 1995; Gerkema, 1996) and fully-nonlinear (Helfrich and Grimshaw, 2008) two-layer modeling, these results reinforce conclusion that underlying nonlinear tide solutions play an important role in the evolution of low-mode internal tides.

These South China Sea examples are also consistent with observations. Lien *et al.* (2005) and Zhao and Alford (2006) have determined that the large amplitude solitary waves observed in the northeastern basin of the South China Sea emerge from the internal tide as it propagates westward from the generation site near Batan Islands in the Luzon Strait. The generating barotropic tides in the Strait have a mixed character with primary semi-diurnal and diurnal components of similar magnitude. Zhao and Alford (2006) show that arrival of large nonlinear internal solitary-like waves at the western side of the basin is linked to phases when the generating tide in Luzon is dominantly semi-diurnal. When the Luzon tide is dominantly diurnal, the large solitary waves are absent. This is broadly what was found in the modeling, though more careful exploration of the problem is needed. In particular, modeling of the generation process is crucial since it sets the parameters of the initial internal tide (e.g., form and amplitude) and can address the question of mixed tides, rather than individual frequencies considered so far. The role of topography on the evolution of the nonlinear tide solutions is also an open issue.

It is important to note that this disintegration process is just the first phase of an interaction between the long intertia-gravity wave and the shorter solitary waves. The first issue is which inertia-gravity wave, of the family of periodic waves at the particular wavelength (or frequency), does the longwave part of the solution initially settle upon? Another concerns the stability of the nonlinear inertia-gravity waves solutions to general small-scale perturbations. The results presented here and in Helfrich and Grimshaw (2008) imply that these waves are quite stable to short waves since the presence of the nonhydrostatic solitary waves does not destroy the long waves. However, for some of the large lobate-class waves (c.f. Fig. 1b and Fig. 10b) the isopycnals slopes approach vertical and stability may be lost. The last is that once the initial disintegration process has halted, the flow will not be a simple superposition of the remaining tide and solitary waves. In one extreme, the short solitary waves may simply be modulated adiabatically by the smoothly varying background flow of the inertia-gravity wave (Gilman *et al.*, 1996). However, the solitary waves will eventually loose energy to the inertia-gravity part of the spectrum (e.g., see Fig. 15b) via a radiation decay process (Grimshaw *et al.*, 1998a). This radiated energy may subsequently be transfered back to short waves through nonlinear steepening (Grimshaw *et al.*, 1998a; Helfrich, 2007). Together, these ideas imply a complex, long-time nonlinear interaction between the nonlinear tides and the shorter solitary waves that requires further study.

Acknowledgments. This work was supported by ONR Grant N000140610798.

REFERENCES

Bell, J. B. and D. L. Marcus. 1992. A second-order projection method for variable-density flows. J. Comput. Phys., *101*, 334–348.

Gerkema, T. 1996. A unified model for the generation and fission of internal tides in a rotating ocean. J. Mar. Res., *54*, 421–450.

Gerkema, T. and J. T. F. Zimmerman. 1995. Generation of nonlinear internal tides and solitary waves. J. Phys. Oceanogr., *25*, 1081–1095.

Gilman, O. A., R. Grimshaw and Y. A. Stepanyants. 1996. Dynamics of internal solitary waves in a rotating fluid. Dyn. Atmos. Oceans, *23*, 403–411.

Grimshaw, R., J.-M. He and L. Ostrovsky. 1998a. Terminal damping of a solitary wave due to radiation in rotational systems. Stud. Appl. Math, *101*, 197–210.

Grimshaw, R. H. J., L. A. Ostrovsky, V. I. Shrira and Y. A. Stepanyants. 1998b. Long nonlinear surface and internal gravity waves in a rotating ocean. Surv. Geophys., *19*, 289–338.

Helfrich, K. R. 2007. Decay and return of internal solitary waves with rotation. Phys. Fluids., *19*, 026601.

Helfrich, K. R. and R. H. J. Grimshaw. 2008. Nonlinear disintegration of the internal tide. J. Phys. Oceanogr., *38*, 686–701.

Helfrich, K. R. and W. K. Melville. 2006. Long nonlinear internal waves. Ann. Rev. Fluid Mech., *38*, 395–425.

Lamb, K. 1994. Numerical experiments on internal wave generation by strong tidal flow across a finite amplitude bank edge. J. Geophys. Res., *99*, 843–864.

Lien, R.-C., T. Y. Tang, M. H. Chang and E. A. D'Asaro. 2005. Energy of nonlinear internal waves in the South China Sea. Geophys. Res. Lett., *32*, L05615, doi:10.1029/2004GL022012.

Lozovatsky, I., E. Morozov and H. Fernando. 2003. Spatial decay of energy density of tidal internal waves. J. Geophys. Res., *108*, doi:10.1029/2001JC001169.

MacKinnon, J. and K. Winters. 2005. Subtropical catastrophe: Significant loss of low-mode tidal energy at 28.9°. Geophys. Res. Lett., *32*, L15605, doi:10.1029/2005GL023376.

Ostrovsky, L. 1978. Nonlinear internal waves in a rotating ocean. Oceanology, *18*, 119–1125.

Pedlosky, J. 1996. Ocean Circulation Theory, Springer, 453 pp.

Plougonven, R. and V. Zeitlin. 2003. On periodic inertia-gravity waves of finite amplitude propagating without change of form at sharp density-gradient interfaces in the rotating fluid. Phys. Lett. A., *314*, 140–149.

Rainville, L. and R. Pinkel. 2006a. Baroclinic energy flux at the Hawaiian Ridge: Observations from the R/P FLIP. J. Phys. Oceanogr., *36*, 1104–1219.

—— 2006b. Propagation of low-mode internal waves through the ocean. J. Phys. Oceanogr., *36*, 1220–1236.

Ramp, S. R., T. Y. Tang, T. F. Duda, J. F. Lynch, A. K. Liu, C.-S. Chiu, F. L. Bahr, H.-R. Kim and Y.-J. Yang. 2005. Internal solitons in the northeastern South China Sea Part I: Sources and deep water propagation. IEEE J. Oceanic Engr., *29*, 1157–1181.

Ray, R. and G. Mitchum. 1996. Surface manifestation of internal tides generated near Hawaii. Geophys. Res. Lett., *23*, 2101–2104.

—— 1997. Surface manifestation of internal tides in the deep ocean. Prog. Oceanogr., *40*, 135–162.

Shrira, V. I. 1986. On long strongly nonlinear waves in a rotating ocean. Izvestiya Atm. Oceanic Phys., *22*, 298–305.

Stanton, T. P. and L. A. Ostrovsky. 1998. Observations of highly nonlinear solitons over the continental shelf. Geophys. Res. Lett., *25*, 2695–2698.

Turner, J. S. 1973. Buoyancy Effects in Fluids, Cambridge University Press, 368 pp.

Wunsch, C. and R. Ferrari. 2004. Vertical mixing, energy, and the general circulation of the oceans. Ann. Revs. Fluid Mech., *36*, 281–314.

Zhao, Z. and M. Alford. 2006. Source and propagation of internal solitary waves in the northeastern South China Sea. J. Geophys. Res., *111*, C11012, doi:10.1029/2006JC003644.

Zhao, Z., V. Klemas, Q. Zheng and X.-H. Yan. 2004. Remote sensing evidence for baroclinic tide origin of internal solitary waves in the northeastern South China Sea. Geophys. Res. Lett., *31*, L06302, doi:10.1029/2003GL019077.

Received: *2 January, 2008*; revised: *6 June, 2008*.